

# On the Electrodeposition of Ca-P Coatings on Nitinol Alloy: A Comparison Between Different Surface Modification Methods

M.R. Etmianfar and J. Khalil-Allafi

(Submitted September 28, 2015; in revised form December 10, 2015; published online January 4, 2016)

In this study, a combination of surface modification process and the electrochemical deposition of Ca-P coatings was used for the modification of the Nitinol shape memory alloy. DSC, SEM, GIB-XRD, FT-Raman, XPS, and FTIR measurements were performed for the characterization of the samples. Results indicated that chemical etching and boiling of the samples in distilled water formed TiO film on the surface. After the chemical modification, subsequent aging of the sample, at 470 °C for 30 min, converted the oxide film to a stable structure of titanium dioxide. In that case, the treated substrate indicated a superelastic behavior. At the same electrochemical condition, the treated substrate revealed more stable and uniform Ca-P coatings in comparison with the abraded Nitinol substrate. This difference was attributed to the presence of hydroxyl groups on the titanium dioxide surface. Also, after soaking the sample in SBF, the needle-like coating on the treated substrate was completely covered with the hydroxyapatite phase which shows a good bioactivity of the coating.

**Keywords** Ca-P coatings, electrochemical deposition, Nitinol, superelasticity, surface modification

## 1. Introduction

NiTi alloys are one of the most important biomaterials due to their unique properties such as superelasticity and shape memory effect (Ref 1, 2). One of the serious concerns in Ni-rich NiTi alloys is release of Ni(II) ions in the vicinity of living body liquids (Ref 3, 4). Not only does Ni(II) ion lead to cells death at the surrounding tissues, but it also forms plaque inside the blood vessels (Ref 5). The bio-inert surface of the alloy is another important issue of NiTi alloys that contribute to some problems in Nitinol implants (Ref 6).

Although calcium phosphate (Ca-P)-based coatings have a considerable effect on improving the bioactivity of the alloy, porous coatings cannot effectively suppress the releasing of Ni ions (Ref 7). As a result, modification of the surface with proper surface treatment methods is necessary for all of the Nitinol implants.

Different surface treatment methods have been introduced for improving the metallic implant performance such as chemical etching, electro-polishing, anodizing, thermal treatment, laser surface treatment, etc (Ref 7-15).

In specific applications, in which thin alloys are used, chemical etching methods seem to be more suitable than the other techniques. In the chemical etching methods, the resulting surface layers are extremely fine (in the nanometric scale); and therefore, this method does not deteriorate the superelastic

property of the alloy. However, to achieve the best results, post-treatment in boiling water or steam is offered in the literature for the complete Ni removing from the surface (Ref 7, 9, 10). The age hardening treatments of NiTi alloys can also be helpful for the surface modification process (Ref 9, 10).

While some contributions can be found in the literature on the electrodeposition of calcium phosphates on Nitinol alloys (Ref 16-18), application of suitable surface treatment process that preserves the superelastic property is not considered in most studies. In the current work, a combination of surface modification process and electrochemical deposition of calcium phosphate coatings was applied for the modification of Nitinol superelastic alloys. After characterizing the surface structure of the modified alloy, the effect of the surface modification method on the electrocrystallization of calcium phosphate-based coatings was investigated.

## 2. Materials and Methods

### 2.1 Preparation of Specimens

In this work, cold-worked NiTi rod with nominal composition of 50.9% Ni was used as substrates. The rods with the diameter of 13 mm were sliced into 1-mm disks. To evaluate the effect of the surface modification on subsequent electrochemical deposition, two types of samples were prepared. In the first type, the surface was abraded with different grades of SiC papers (Only Abraded sample, O.A.). In the second type, the surface was abraded with different grades of SiC papers from P80 to P600 grit and then was etched in a 1HF-4 NHO<sub>3</sub>-5 H<sub>2</sub>O solution for 4 min, and finally was soaked in distilled boiling water for 20 min (Chemically etched and Boiled sample, C.B.). After each step, specimens were cleaned in acetone and then rinsed with deionized water. For the heat treatment process, the C.B. samples were encapsulated in a

M.R. Etmianfar and J. Khalil-Allafi, Research Center for Advanced Materials, Faculty of Materials Engineering, Sahand University of Technology, Tabriz, Iran. Contact e-mail: allafi@sut.ac.ir.

glass tube after purging and vacuuming the high-purity Ar gas inside it for several times. The heat treatment was carried out at 470 °C for 30 min (C.B.H. samples).

## 2.2 Electrochemical Deposition

An electrolyte solution of 0.042 M  $\text{Ca}(\text{NO}_3)_2 \cdot 4\text{H}_2\text{O}$  and 0.025 M  $\text{NH}_4\text{H}_2\text{PO}_4$  and 6 mL/L  $\text{H}_2\text{O}_2$  was prepared and used for the electrodeposition of calcium phosphate.

The pH of the electrolyte was 4.3, and the temperature of the electrolyte was maintained at  $70 \pm 1$  °C using Bain-Marie method. Mechanical stirring of the electrolyte was controlled at a speed of 150 rpm during the deposition process. The electrodeposition was performed in an individual cell using a regular three-electrode configuration in which NiTi alloy served as the cathode and a platinum mesh acts as the anode. The deposition was carried out in galvanostatic mode and the current density was maintained at 0.6 mA/cm<sup>2</sup>.

## 2.3 Characterization of Modified Samples and Coatings

For the roughness measurement, Taylor Hobson-Surtronic25-UK device was used. The evaluation length and the gage length of test were 4.00 and 0.80 mm, respectively. At least, the average of five measurements was used to report the results.

For the evaluation of phase changes in modified samples, the DSC measurements were performed using NETZSCH 404C-Germany calorimeter with 30 °C/min heating rates in the temperature range of 50 to 500 °C.

The crystalline state of the surface films was examined by a PANalytical-X'Pert Pro MPD-Netherlands XRD device with  $\text{Cu K}_\alpha$  radiation generated at 40 kV, 40 mA, and in Grazing Incidence Beam (GIB) mode with the incident beam angle of 1°. Data collection was done over the  $2\theta$  range of 20 to 120° with a step size of 0.04° and a step time of 100 s. Also, the structure of the calcium phosphate-based coating was analyzed by x-ray diffraction (XRD) using BRUKER-D8 Advance-Germany Spectrometer, with  $\text{Cu K}_\alpha$  radiation generated at 40 kV and 40 mA. Data were collected over the  $2\theta$  range of 10° to 70° with a step size of 0.01° and a step time of 1 s.

The micro-Raman spectra were recorded on a LabRam confocal Raman microscope with a 300-mm focal length. The spectrometer was equipped with a Ventus LP 532, 50 mW, diode-pumped solid-state laser operator at 20 mW, with a polarization ratio of 100:1, a wavelength of 532.1 nm, and a  $1024 \times 256$  element CCD camera. The collected signal was transmitted via a fiber optic cable into a spectrometer with 600 g/mm grating. The Raman spectra were collected by manually placing the probe tip on the desired point of the sample over the substrate.

The superelastic behavior of the treated sample was studied using a Santam (STM50) tensile testing instrument at 37 °C and a cross-head speed of 0.1 mm/min in a loading and unloading course up to 5.5% strain. Overall length of the sample between the grasps was 60 mm.

X-ray photoelectron spectroscopy (XPS) analysis was performed with a PHI 5000 Versa Probe spectrometer (F ULVACPHI Inc., Japan/USA) using monochromatized  $\text{Al K}\alpha$  radiation (1486.6 eV) as an x-ray source with a 45° electron collection angle.

The chronopotentiometry measurements were recorded using GAMRY, PCI4G750 (USA) instrument.

For the electrodeposited samples on Nitinol substrates, ATR-FTIR measurements were carried out on Bruker alpha

(Germany) platinum ATR equipped with diamond crystal. The spectra were recorded between 400 and 4000 cm<sup>-1</sup> and resolution of 4.0 cm<sup>-1</sup> by accumulation of 130 scan.

The surface morphology and the composition of deposited films were examined by a CamScan MV2300-Czech scanning electron microscope (SEM) with an energy dispersive spectroscopy (EDS) analyzer. Also FEI-Quanta 400 FE6-Netherlands field emission SEM was used for observing the coatings in the higher magnifications. The operating voltage in SEM studies was 20.0 kV.

The bioactivity of the Ca-P coating was investigated by immersing the coated sample in simulated body fluid (SBF) for 7 days at 37 °C. The SBF was prepared according to Kokubo's instruction (Ref 19, 20) and it was buffered to pH 7.4 at 37 °C by adding 1 M HCl and Tris (hydroxymethyl aminomethane). In order to stabilize the ion concentration and the pH value of SBF, the solution was refreshed each 2 days.

## 3. Results and Discussion

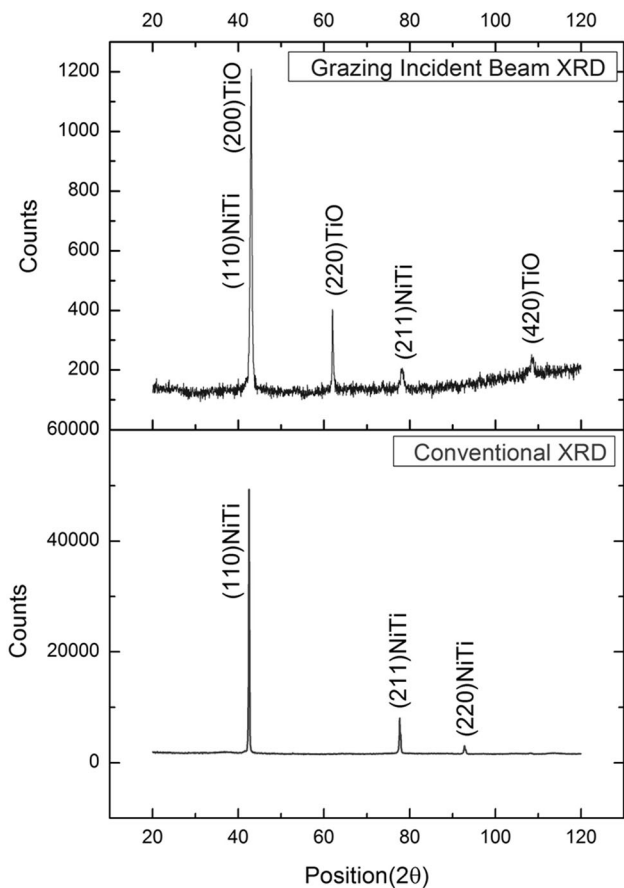
### 3.1 Characterization of Treated Surfaces

Figure 1 shows the GIB and conventional XRD diffraction patterns of the C.B. sample. According to the GIB analysis, In addition to the peaks of the substrate (conventional XRD), the film on the C.B. sample contains titanium oxides in the form of TiO. Probably, because of the high affinity of titanium to the oxygen, the titanium mono oxide layer is formed on the alloy as a result of the Ni ions dissolution during the chemical treatment process. However, as a result of the ambient temperature of the process, the produced oxide film is not in a stable form.

Figure 2 shows DSC results for the NiTi samples in two different surface conditions of the O.A. and C.B. The first peak in Fig. 2, which is seen for the both surface conditions, is probably due to the recovery process of pervious cold workings. Considering this figure, another exothermic peak can be also detected in the curve of the C.B. sample. To investigate the second peak reaction, x-ray diffraction analysis was carried out on the C.B.H. sample. Figure 3 shows the obtained patterns of GIB and conventional XRD analysis at 22 °C.

Comparing the patterns of Fig. 1 and 3 reveals that during the aging process, some precipitates and martensite phase are formed in the bulk of the alloy. Also the surface oxide films are converted to the stable form of TiO<sub>2</sub>. Accordingly, the second exothermic reaction in Fig. 2 is probably related to the structural changes of the surface oxide film. This exothermic reaction is not seen for the O.A. sample probably because of the lack of TiO film on the sample after the abrading process. Another observation in Fig. 3 is the preferred orientation of titanium oxide on the Nitinol alloy surface. This may be related to the preferred orientation of the base metal (conventional XRD of Fig. 1 and 3) or it happens in line with the minimum interface energy between the oxide film and the substrate.

The results of the roughness measurement for the O.A., C.B., and C.B.H. samples are listed in Table 1. According to Table 1, the sign of Rsk (skewness) changes in different surface conditions. Rsk shows the depth of valley and the height of peaks in the roughness profile. The positive sign of the parameter shows that the peaks' height is more than valleys' depth and the negative sign shows that the valleys are deeper



**Fig. 1** GIB and conventional XRD patterns for the NiTi sample after the chemical etching for 4 min and boiling in distilled water for 20 min (C.B. sample)

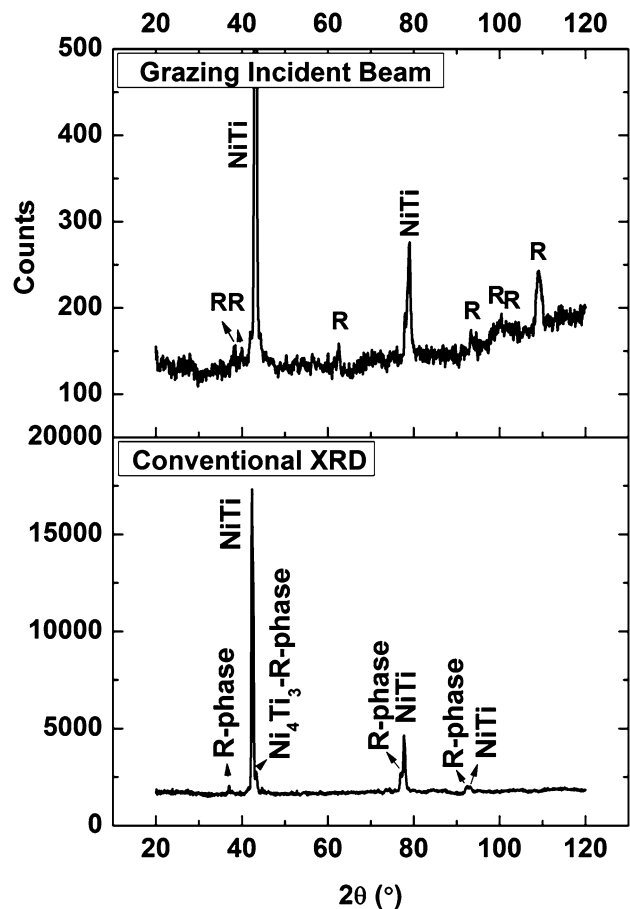


**Fig. 3** GIB and conventional XRD patterns for the C.B.H. sample (R: Rutile, R-phase martensite phase of Nitinol)

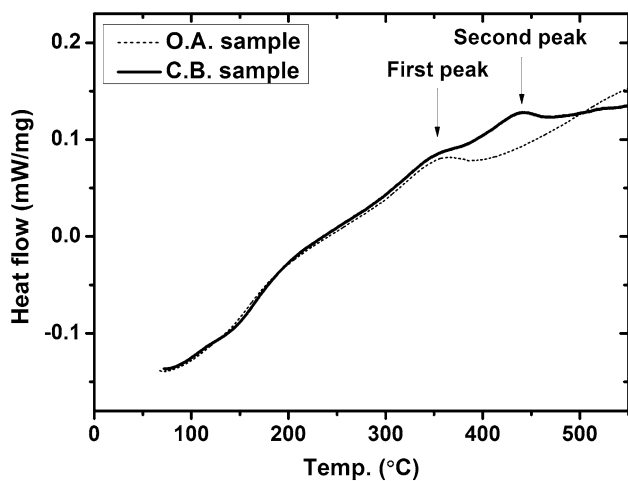


**Fig. 2** DSC results of the O.A. and C.B. samples under Ar gas atmosphere

than the peaks (Ref 21). Accordingly, in the C.B. and C.B.H. samples, surface profile is composed of deep valleys.

The Raman spectra of the Nitinol alloy, obtained by different surface treatment steps, are depicted in Fig. 4. As seen, after the chemical etching and boiling process, some undefined peaks appear in the Raman spectra. Probably these

**Table 1** Roughness measurement data of NiTi samples after different surface treatment processes

Parameters/treatments	O.A.	C.B.	C.B.H.
Ra	0.44	0.42	0.74
Rz	3.4	4.8	6.7
Rsk	0.31	-3.46	-2.87

peaks are related to the oxide layer of the treated alloy. After the heat treatment process (C.B.H. sample), TiO<sub>2</sub> peaks can also be seen in the spectrum indicating the presence of rutile on the surface of the alloy. The principal features of the spectra are the bands at Raman shifts of 146, 448, and 612 cm<sup>-1</sup>. These bands correspond to the normal positions of the rutile phase of TiO<sub>2</sub>. In this sample, another band between 210 and 300 cm<sup>-1</sup> is also observed. The asymmetric peak shape suggests that it is composed of more than one peak. The band at the Raman shift of 236 cm<sup>-1</sup> is also related to rutile phase. The remaining bands around ~250 cm<sup>-1</sup> and the band in the range of 320 to 360 cm<sup>-1</sup> are related either to disorder induced scattering or second-order scattering of rutile structure (Ref 22, 23).

The stress-strain curve of the C.B.H. sample is shown in Fig. 5. Despite the presence of the oxide film, the alloy shows a superelastic property at the human body temperature after the treatment process.

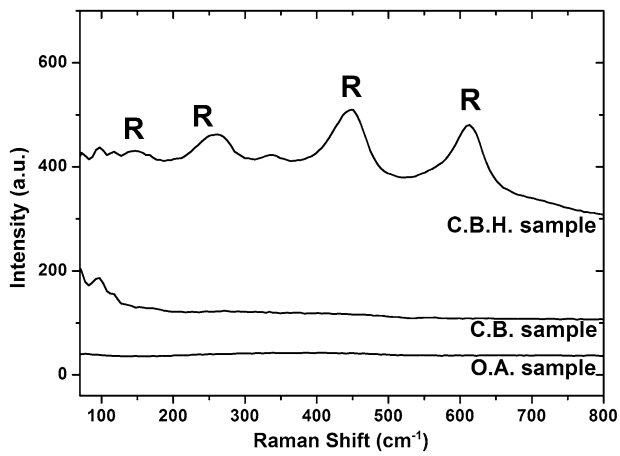


Fig. 4 Raman spectra of the Nitinol superelastic alloy after different surface treatments of O.A., C.B., and C.B.H. (R: Rutile)

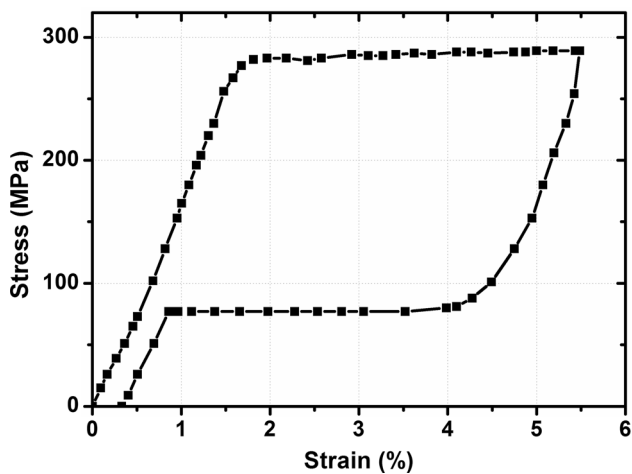
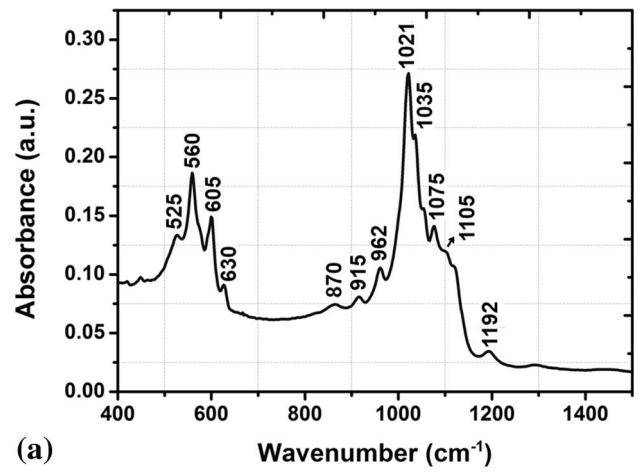


Fig. 5 Stress-strain curve of the C.B.H. sample at 37 °C

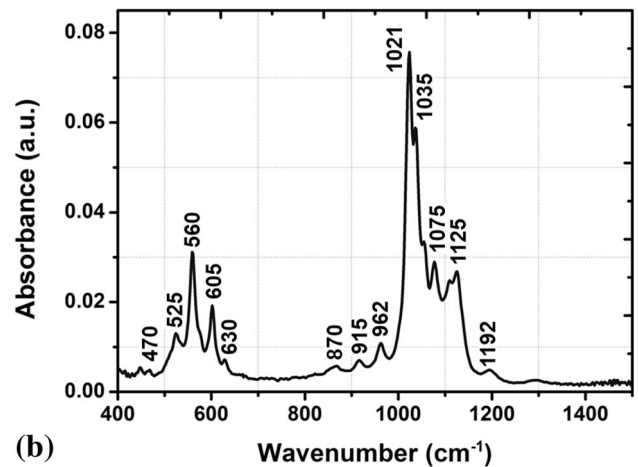
### 3.2 Electrodeposition of Ca-P coatings

The related ATR-FTIR spectra of the 5 min electrodeposited coatings on the O.A. and C.B.H. substrates are illustrated in Fig. 6. In these spectra, the infrared bands at 470, 560, 605, 865, 962, 1021, 1035, and 1125  $\text{cm}^{-1}$  correspond to  $\text{PO}_4^{3-}$  bands and the weak or shoulder peaks at 525, 1075, 1105, and 1192  $\text{cm}^{-1}$  are assigned to biphosphate groups ( $\text{HPO}_4^{2-}$ ). Also, in both spectra, the OH and carbonate bands can be observed at 630 and 870  $\text{cm}^{-1}$ , respectively (Ref 24-28). Comparing Fig. 6a with b reveals that a distinct phosphate group bands at 470 and 1125 are only seen in the coating of the treated substrate. The data show that beside the similar electrodeposition condition for both substrates, more phosphate groups can be generated on the C.B.H. substrate in comparison with that of the O.A. substrate.

Analyzing the high-resolution XPS spectra of O1s (Fig. 7) shows that oxides and hydroxyl groups are present in the outermost layer of the C.B.H. substrate. Hydroxyl groups can act as nucleation sites for calcium phosphates. Equation 1 shows the reaction between calcium ions and hydroxyl groups. It has been known that adsorption of calcium divalent cations, at alkaline pH values, converts the surface charge of rutile from



(a)



(b)

Fig. 6 ATR-FTIR spectra of the calcium phosphate coatings on various surface conditions of (a) O.A. sample, and (b) C.B.H. sample

negative to positive (Ref 29). Consequently, the positively charged surface will attract the negatively charged phosphate and hydroxyl groups, which results in the formation of Ca-P nucleolus.

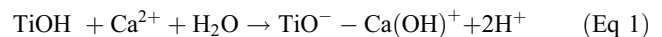


Figure 8 shows chronopotentiometry results of the O.A. and C.B.H. substrates at the same electrochemical condition. For the O.A. substrate, the start point of the potential is  $-0.45$  V (vers. Ag/AgCl). It remains constant during  $\sim 2$  min and after that the value of the potential starts to increase up to  $-0.39$  V. As can be seen, after this step, a slope change happens after approximately 8 min. On the treated substrate, the potential starts to decrease continually from  $-0.25$  V (vers. Ag/AgCl) to the negative values.

Visual analyzing of the films on the different surface conditions revealed that a uniform coating is formed on the treated substrate after several minutes but in the abraded substrate, the surface coverage is poor (Fig. 9). Since the treated sample has a high density of nucleation sites, the nucleation process of calcium phosphates is carried out with lower barrier energy for crystallization in comparison with that

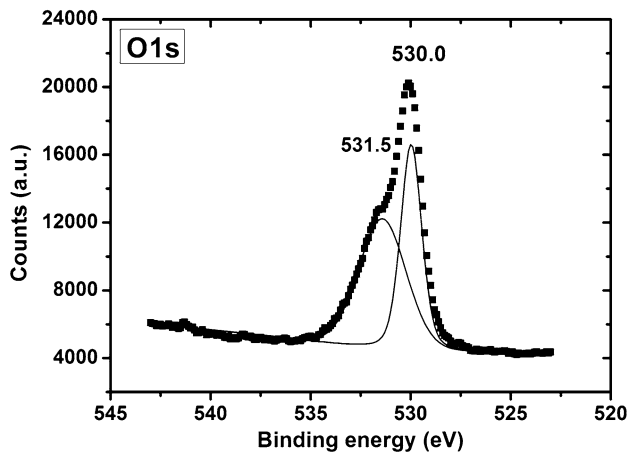


Fig. 7 O1s high-resolution XPS spectra of C.B.H. sample

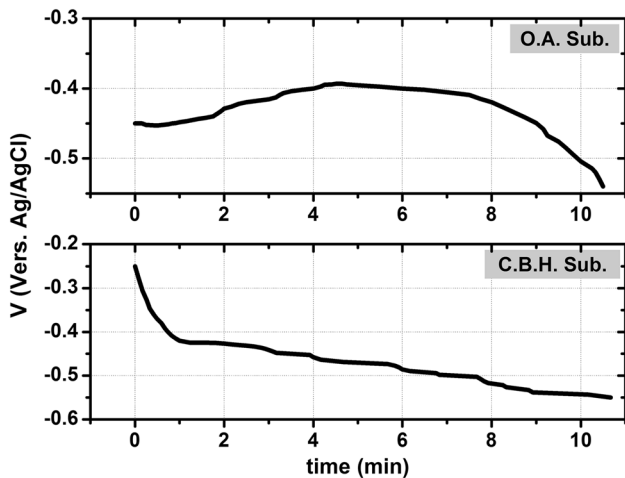
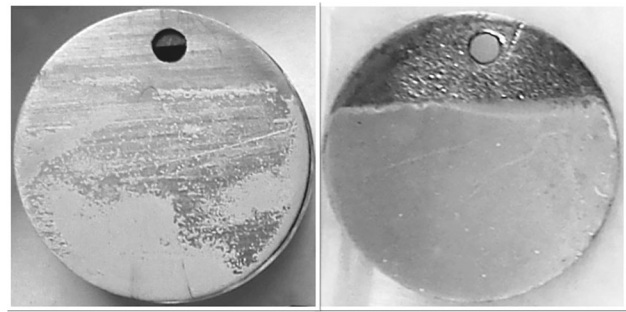


Fig. 8 Chronopotentiometry results for the O.A. and C.B.H. substrates at the same electrochemical conditions of the deposition process

of the O.A. sample (Ref 30). Accordingly, the entire surface of the treated substrate is covered with the coating rapidly in a low applied potential. Considering that the coating has an electrical resistance, the absolute value of the cathodic potential gradually increases by increasing the time and the coating thickness.

On the other hand, the nucleation on the abraded substrate needs a high energy and some precipitates nucleate, especially at the edges, after supplying the required potential. Since the crystallization on the precipitates needs smaller energy than that of the initial nucleation, the absolute value of the cathodic potential starts to decrease after this step (Ref 30). After the surface coverage with the coating (~8 min), continuous increase in the potential can be seen in the diagram of chronopotentiometry.

Figure 10 shows the surface morphologies and cross-sectional images of the deposited samples after 30 min of electrodeposition time. Although the thicknesses of coatings are almost the same, the coating of O.A. substrate shows cracks on the surface and delamination of coatings can be seen in some region. Although the surface is covered by the coating during



(a) (b)

Fig. 9 Surface coverage of calcium phosphate coatings on the (a) O.A. sample, and (b) C.B.H. sample

the deposition, the reduction reactions can occur at the interface because of the porosity of coatings. It seems that the observed degradation of the coating can be attributed to the hydrogen evolution at the interface.

Considering Fig. 10b, although the track of hydrogen bubbles can be seen on the coating of the C.B.H. substrate, this process did not destruct the coating. It seems that, because of the specific surface profile on the C.B.H. sample, the electrochemically deposited calcium phosphate coating is formed initially at the valleys and this acts as a root for the overall coating. As a result, the deposited film is more uniform in comparison with the film formed on O.A. substrate. Also, it should be considered that beside the surface profile of the samples, crystal structure and oxidation state of the surface are the other important factors in the bonding and crystallization of coatings on the substrates (Ref 16, 31-34).

### 3.3 Bioactivity of the Ca-P Coating on the C.B.H. Substrate

High-resolution SEM micrographs of the Ca-P coating on the C.B.H. substrate are shown in Fig. 11. The coating shows needle-like morphology which is predominate morphology and also there are some plate-like structures in the coating. Analyzing of the Ca/P ratio by EDS revealed that the plate-like structures have a higher Ca/P ratio (1.65) in comparison with the base coating (1.4). FE-SEM image shows that the needles on the coating have a flattened shape and actually they are strips with an ultrafine thickness. It was shown that strip-shaped crystals have a higher value of Ca/P ratio in comparison with the round-shaped crystals (Ref 35). It seems that in some areas, the strips have an opportunity to grow up, and as a result, the plate-like structures are formed in the coating.

Figure 12a shows the XRD patterns of the electrodeposited sample. It can be seen that beside the hydroxyapatite (HA) phase, some other compounds like octa calcium phosphate and brushite are also formed during the electrodeposition.

The Ca-P phases with a lower Ca/P ratio than hydroxyapatite can be converted to HA by a dissolution and precipitation process. The ability of apatite formation can be estimated using immersion of samples in SBF (Ref 36). The surface morphology of the coated sample on the C.B.H. substrate after immersion in SBF is depicted in Fig. 13. It can be seen that the sample is completely covered by HA crystals after immersion in SBF for one week. Figure 12b shows XRD

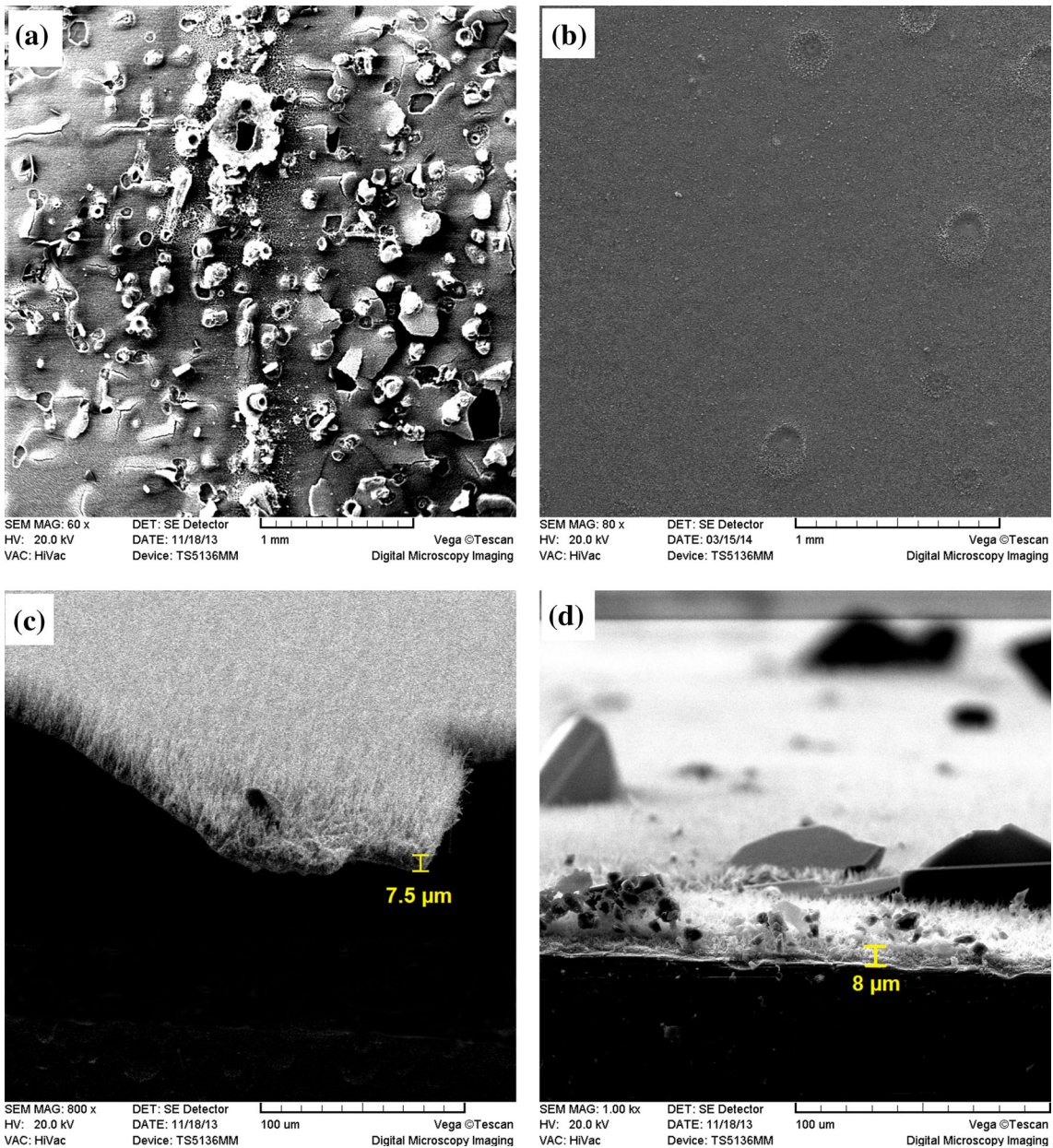


**Fig. 10** Surface morphologies and cross-sectional images of calcium phosphate coatings electrodeposited on the (a) and (c) O.A. sample, (b) and (d) C.B.H. sample

pattern of the coating after the immersion test. According to the pattern, the unstable phases are eliminated during soaking in SBF and the resulted film is composed of HA crystals.

#### 4. Conclusion

In this study, a thermo-chemical surface treatment is applied on Nitinol alloys. Based on the results of this work, after the

chemical etching and boiling in distilled water, the surface of the NiTi alloy is converted to TiO oxide. The age hardening process of the chemically modified NiTi alloy, at 470 °C for 30 min, results in conversion of the surface oxide film to the stable structure of titanium dioxide. The treated alloy indicates a good superelastic behavior. Also, the treated substrate offers more sites to the crystallization of Ca-P coatings and the resulted film contains more phosphatic phases in comparison with that of the abraded Nitinol substrate. In addition, this surface condition results in the formation of Ca-P coatings with the morphology of ultra fine strips. As the immersion test in

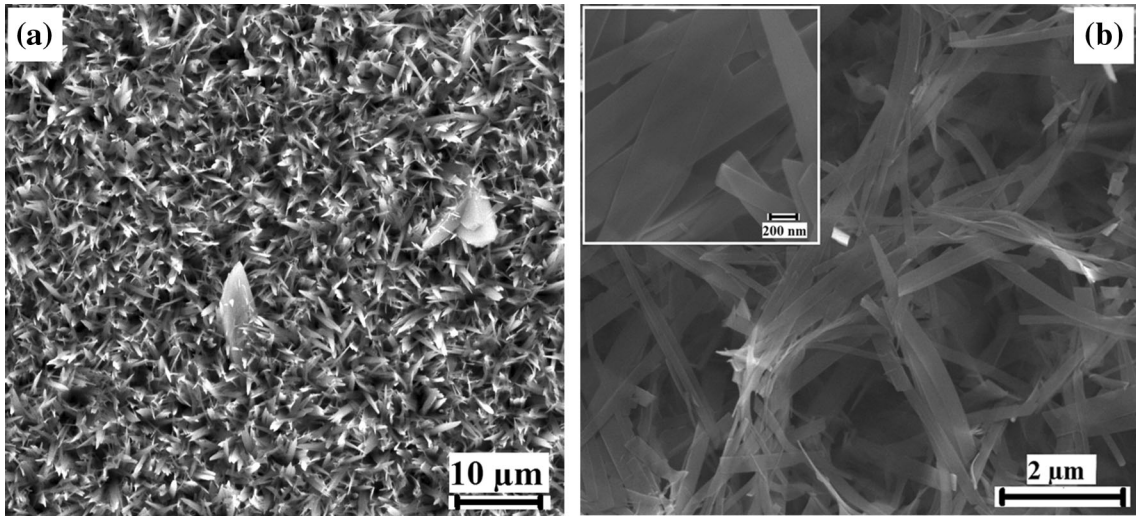


Fig. 11 (a) SEM, and (b) FE-SEM micrographs of the calcium phosphate coating electrodeposited on C.B.H. sample

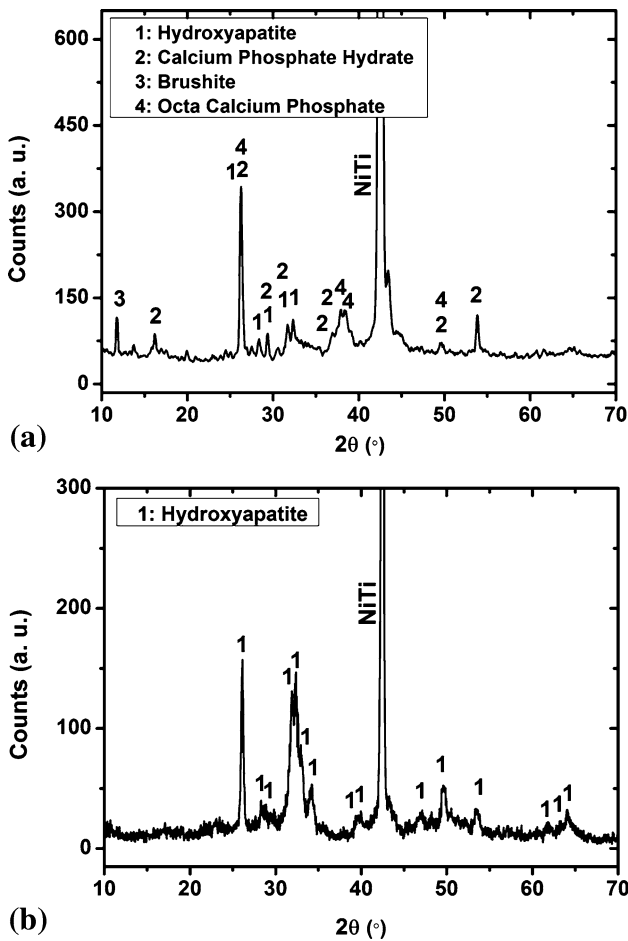


Fig. 12 XRD patterns of the Ca-P coating on the C.B.H. sample, (a) after deposition, and (b) after soaking the sample in S.B.F. for one week at 37 °C

SBF confirms, the Ca-P coating on the treated substrate shows a good bioactivity, and after the test, a crystalline HA phase is formed on the coating.

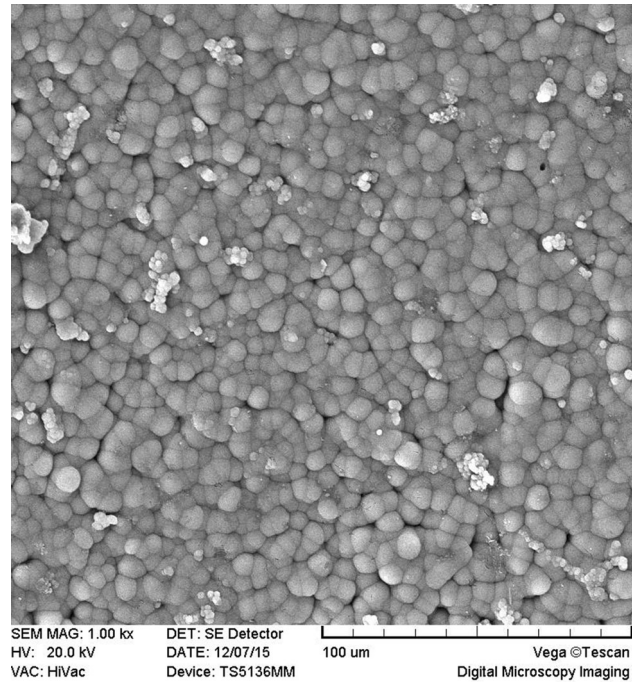


Fig. 13 The surface morphology of the coated sample on the C.B.H. substrate after immersion in SBF for one week at 37 °C

### Acknowledgments

The authors would like to acknowledge the financial support from the Iran National Science Foundation (INSF) under the contract No. 92004023. Also the authors acknowledge Prof. Ö. Dag from Bilkent University, Turkey for ATR-FTIR and Raman studies.

### References

1. A.R. Pelton, D. Stockel, and T.W. Duerig, Medical Uses of Nitinol, *Mater. Sci. Forum*, 2000, **327**, p 63–70

2. M.H. Elahinia, M. Hashemi, M. Tabesh, and S.B. Bhaduri, Manufacturing and Processing of NiTi Implants, *Prog. Mater. Sci.*, 2012, **57**, p 911–946
3. H. Tian, D. Schryvers, D. Liu, Q. Jiang, and J.V. Humbeeck, Stability of Ni in Nitinol Oxide Surfaces, *Acta Biomater.*, 2011, **7**, p 892–899
4. J.L. Xu, F. Liu, F.P. Wang, D.Z. Yu, and L.C. Zhao, Formation of Al<sub>2</sub>O<sub>3</sub> Coatings on NiTi Alloy by Micro-Arc Oxidation Method, *Curr. Appl. Phys.*, 2009, **9**, p 663–666
5. S.D. Plant, D.M. Grant, and L. Leach, Surface Modification of NiTi Alloy and Human Platelet Activation Under Static and Flow Conditions, *Mater. Lett.*, 2007, **61**, p 2864–2867
6. Z.D. Cui, M.F. Chen, L.Y. Zhang, R.X. Hu, S.L. Zhu, and X.J. Yang, Improving the Biocompatibility of NiTi Alloy by Chemical Treatments: An In Vitro Evaluation in 3T3 Human Fibroblast Cell, *Mater. Sci. Eng. C*, 2008, **28**, p 1117–1122
7. S. Shabalovskaya, J. Anderegg, and J. Van Humbeeck, Critical Overview of Nitinol Surfaces and their Modifications for Medical Applications, *Acta Biomater.*, 2008, **4**, p 447–467
8. H. Maleki-Ghaleh, J. Khalil-Allafi, E. Aghaie, and M.H. Siadati, Effect of TiO<sub>2</sub>-Ti and TiO<sub>2</sub>-TiN Composite Coatings on Corrosion Behavior of NiTi Alloy, *Surf. Interface Anal.*, 2015, **47**, p 99–104
9. H. Kheimehsari, S. Izman, and M. Rezaadeh-Shirdar, Effects of HA-Coating on the Surface Morphology and Corrosion Behavior of a Co-Cr-Based Implant in Different Conditions, *J. Mater. Eng. Perform.*, 2015, **24**(6), p 2294–2302
10. S. Paul and Ch Mandal, Biocompatibly Coated 304 Stainless Steel as Superior Corrosion-Resistant Implant Material to 316L Steel, *J. Mater. Eng. Perform.*, 2013, **22**(10), p 3147–3154
11. R.M. Oliveira, B.B. Fernandes, F.C. Carreri, J.A.N. Gonçalves, M. Ueda, M.M.N.F. Silva, M.M. Silva, L. Pichon, E.N. Camargo, and J. Otubo, Surface Modification of NiTi by Plasma Based Ion Implantation for Application in Harsh Environments, *Appl. Surf. Sci.*, 2012, **263**, p 763–768
12. ChK Lee, Fabrication, Characterization and Wear Corrosion Testing of Bioactive Hydroxyapatite/Nano-TiO<sub>2</sub> Composite Coatings on Anodic Ti–6Al–4V Substrate for Biomedical Applications, *Mater. Sci. Eng. B*, 2012, **177**, p 810–818
13. H.T. Siu and H.C. Man, Fabrication of Bioactive Titania Coating on Nitinol by Plasma Electrolytic Oxidation, *Appl. Surf. Sci.*, 2013, **274**, p 181–187
14. A. Roy, S.S. Singh, M.K. Datta, B. Lee, J. Ohodnicki, and P.N. Kumt, Novel Sol–Gel Derived Calcium Phosphate Coatings on Mg4Y Alloy, *Mater. Sci. Eng. B*, 2011, **176**, p 1679–1689
15. C. Bayram, M. Demirbilek, E. Yalçın, M. Bozkurt, M. Doğan, and E.B. Denkbaş, Osteoblast Response on co-modified Titanium Surfaces via Anodization and Electrospinning, *Appl. Surf. Sci.*, 2014, **288**, p 143–148
16. D. Qiu, L. Yang, Y. Yin, and A. Wang, Preparation and Characterization of Hydroxyapatite/Titania Composite Coating on NiTi Alloy by Electrochemical Deposition, *Surf. Coat. Technol.*, 2011, **205**, p 3280–3284
17. A.O. Lobo, J. Otubo, J.T. Matsushima, and E.J. Corat, Rapid Obtaining of Nano-Hydroxyapatite Bioactive Films on NiTi Shape Memory Alloy by Electrodeposition Process, *J. Mater. Eng. Perform.*, 2011, **20**, p 793–797
18. J. Katic, M. Metikos-Hukovic, and R. Babic, Synthesis and Characterization of Calcium Phosphate Coatings on Nitinol, *J. Appl. Electrochem.*, 2014, **44**, p 87–96
19. A. Oyane, H.M. Kim, T. Furuya, T. Kokubo, T. Miyazaki, and T. Nakamura, Preparation and Assessment of Revised Simulated Body Fluids, *J. Biomed. Mater. Res.*, 2002, **65A**, p 188–195
20. H. Maleki-Ghaleh, V. Khalili, J. Khalil-Allafi, and M. Javidi, Hydroxyapatite Coating on NiTi Shape Memory Alloy by Electrophoretic Deposition Process, *Surf. Coat. Technol.*, 2012, **208**, p 57–63
21. I. M. Hutchings, *Tribology Friction and Wear of Engineering Materials*, 1992 (Great Britain), British Library Cataloguing in Publishing data, 1992
22. S. Mandl, G. Thorwarth, M. Schreck, B. Stritzker, and B. Rauschenbach, Raman Study of Titanium Oxide Layers Produced with Plasma Immersion Ion Implantation, *Surf. Coat. Technol.*, 2000, **125**, p 84–88
23. P.A. Venz, J.T. Klopogge, and R.L. Frost, Chemically Modified Titania Hydrolysates: Physical Properties, *Langmuir*, 2000, **16**, p 4962–4968
24. D.Y. Lin and X.X. Wang, ELECTRODEPOSITION of Hydroxyapatite Coating on CoNiCrMo Substrate in Dilute Solution, *Surf. Coat. Technol.*, 2010, **204**, p 3205–3213
25. E.A. dos Santos, M.S. Moldovan, L. Jacomine, M. Mateescu, J. Werckmann, K. Anselme, P. Mille, and H. Pelletier, Oriented Hydroxyapatite Single Crystals Produced by the Electrodeposition Method, *Mater. Sci. Eng. B*, 2010, **169**, p 138–144
26. R. Hu, ChJ Lin, and H.Y. Shi, A Novel Ordered Nano Hydroxyapatite Coating Electrochemically Deposited on Titanium Substrate, *J. Biomed. Mater. Res.*, 2007, **80A**, p 687–692
27. D.T.M. Thanh, PhT Nam, N.T. Phuong, L.X. Que, N.V. Anh, T. Hoang, and T.D. Lam, Controlling the Electrodeposition, Morphology and Structure of Hydroxyapatite Coating on 316L Stainless Steel, *Mater. Sci. Eng. C*, 2013, **33**, p 2037–2045
28. M. Shirkhazadeh, Direct Formation of Nanophase Hydroxyapatite on Cathodically Polarized Electrodes, *J. Mater. Sci. Mater. Med.*, 1998, **9**, p 67–72
29. H.M. Jang and D.W. Fuerstenau, The Specific Adsorption of Alkaline-Earth Cations at the Rutile/Water Interface, *Colloids Surf.*, 1986, **21**, p 235–257
30. N. Kanani, *Electroplating Basic, Principle and practice*, 2004 (Great Britain), Elsevier, 2004
31. J.H. Park, D.Y. Lee, K.T. Oh, Y.K. Lee, and K.N. Kim, Bioactive Calcium Phosphate Coating on Sodium Hydroxide-Pretreated Titanium Substrate by Electrodeposition, *J. Am. Ceram. Soc.*, 2004, **87**(9), p 1792–1794
32. A. Roguska, M. Pisarek, M. Andrzejczuk, M. Dolata, M. Lewandowska, and M. Janik-Czachor, Characterization of a Calcium Phosphate–TiO<sub>2</sub> Nanotube Composite Layer for Biomedical Applications, *Mater. Sci. Eng. C*, 2011, **31**, p 906–914
33. P.A. Ramires, A. Romito, F. Cosentino, and E. Milella, The Influence of Titania/Hydroxyapatite Composite Coatings on In Vitro Osteoblasts Behavior, *Biomater.*, 2001, **22**, p 1467–1474
34. D. Wei, Y. Zhou, Y. Wang, and D. Jia, Effect of Dehydration on Structure and Induction Capability for Apatite Formation of Microarc Oxidized TiO<sub>2</sub>-Based Film with Chemical Modification, *Thin Solid Films*, 2008, **516**, p 6413–6420
35. Noam Eliaz and T.M. Sridhar, Electrocrystallization of Hydroxyapatite and Its Dependence on Solution Conditions, *Cryst. Growth Des.*, 2008, **8**(11), p 3965–3977
36. S.L. Zhu, X.J. Yang, and Z.D. Cui, Formation of Ca–P Layer on the Ti-Based Bulk Glassy Alloy by Chemical Treatment, *J. Alloys Compd.*, 2010, **504**, p S168–S171